



Internal vortex breakdowns with stair-step change in rotating flows

Cite as: Phys. Fluids **34**, 093613 (2022); <https://doi.org/10.1063/5.0107296>

Submitted: 04 July 2022 • Accepted: 01 September 2022 • Accepted Manuscript Online: 02 September 2022 • Published Online: 23 September 2022

 Cong Li (李丛),  Jiping Huang (黄吉平), Weijuan Fu (符维娟), et al.



View Online



Export Citation



CrossMark

ARTICLES YOU MAY BE INTERESTED IN

[Wall-attached and wall-detached eddies in proper orthogonal decomposition modes of a turbulent channel flow](#)

Physics of Fluids **34**, 095124 (2022); <https://doi.org/10.1063/5.0105478>

[Steady Flow of Power-Law Fluids past a Slotted Circular Cylinder at Low Reynolds Number](#)

Physics of Fluids (2022); <https://doi.org/10.1063/5.0102861>

[Computational fluid dynamics characterization of the hollow-cone atomization: Newtonian and non-Newtonian spray comparison](#)

Physics of Fluids **34**, 093318 (2022); <https://doi.org/10.1063/5.0104658>

Physics of Fluids

Submit Today!

Special Topic: Hydrogen Flame and Detonation Physics



Internal vortex breakdowns with stair-step change in rotating flows

Cite as: Phys. Fluids **34**, 093613 (2022); doi: [10.1063/5.0107296](https://doi.org/10.1063/5.0107296)

Submitted: 4 July 2022 · Accepted: 1 September 2022 ·

Published Online: 23 September 2022



View Online



Export Citation



CrossMark

Cong Li (李丛),^{1,a)}  Jiping Huang (黄吉平),²  Weijuan Fu (符维娟),² Ge Song (宋戈),¹  Yingli Chang (常英立),¹ and Zigen Song (宋自根)¹

AFFILIATIONS

¹College of Information Technology, Shanghai Ocean University, Shanghai 201306, China

²Department of Physics, State Key Laboratory of Surface Physics, and Key Laboratory of Micro and Nano Photonic Structures (MOE), Fudan University, Shanghai 200438, China

^{a)}Author to whom correspondence should be addressed: cli@shou.edu.cn

ABSTRACT

Understanding internal vortex breakdowns (VBs) and their trajectories in sealed cylinders are important for the scientific and industrial applications with which they are linked. However, the fluids in sealed cylinders are often sheared, which makes it difficult to clearly and multidirectionally observe their internal flow patterns simultaneously with existing experimental tools; this results in some important features not being captured. In this work, we performed thousands of numerical simulations in a sealed cylinder utilizing the finite element approach. Abundant internal VB patterns were obtained for different aspect ratios as the Reynolds number (Re) increased. To further quantitatively study the morphological evolution of VBs, we focused on the axial lengths and trajectories of VBs with multiple aspect ratios. Surprisingly, the numbers of VBs in the rotating fluid were not fixed for the same aspect ratio, which also affected the complexity of the VB evolution. In particular, the stair-step changes of the locations of the VB and local extrema of the axial velocity, pressure, and vorticity of the key flows at the axis were revealed in detail. We used the theory of swirl decay to explain the VB formation and stair-step change from an energy perspective and clarified why the pressure minimum was under the center of the VB. The discovery of the stair-step change of the VB provided evidence of the existence of a new class of fluid behavior that may provide insight into vortex control.

© 2022 Author(s). All article content, except where otherwise noted, is licensed under a Creative Commons Attribution (CC BY) license (<http://creativecommons.org/licenses/by/4.0/>). <https://doi.org/10.1063/5.0107296>

I. INTRODUCTION

Fluid, existing everywhere, has a close relationship with human life and production, so it is of particular importance to study and control fluid flow.^{1–6} Together with the rapid development of engineering and thermal energy control,^{7–13} vortex research has gradually become a powerful tool for fluid control, which began from the unexpected reverse flow that occurs in the center of a pipe.¹ In general, vortex research can be used to reveal new fluid behaviors and develop new applications. Until now, a large number of studies have been conducted on fluid structures, behaviors, and mechanisms,^{1–3,14–42} vortex-induced diffusion, fusion and reaction,^{7,43–47} and industrial applications.^{48–51}

Recently, researchers have shown an increased interest in vortex study, especially vortex breakdown (VB).^{6,7,14–16,30,32,33,35–39,41,45,46,51–59} The topologies of VB were thought to be too unstable to actually occur.⁴¹ The design of a pappus stabilized one separate vortex ring (also called VB) at 60% of the terminal velocity.⁷ However, a continuum

description that captures the important features of multiple VBs, such as the morphology and propagation characteristics under complex conditions, is not yet at hand. This issue in rotating fluids may be addressed by the study of flows in sealed cylinders.^{14,15,19,22,25,42} Lid-driven cylinders are internal flow type cylinders with simple geometry and complex flow nature.³¹ Although the system in this geometry is fully three-dimensional, the invariance of the equations and boundary conditions to arbitrary rotations in the azimuthal direction naturally provides a periodic direction that can be efficiently exploited in the solution scheme. This simple geometry and absence of ambient disturbances allow both experimental and numerical studies to be conducted to help understand vortex dynamics. 37 Escudier¹⁷ carried out the most detailed experimental study of rotating flows in a sealed cylinder by employing a laser-induced fluorescence technique. He found that three axisymmetric distinct breakdown bubbles can occur with different values of the model parameters, the aspect ratio, and the Reynolds number (Re).

To date, traditional investigations of vortices in experiments tend to observe a single axisymmetric profile, and it is difficult to observe the radial section simultaneously due to the limitations of instruments. At the same time, the dye filament can be confused with the vortex core, which leads to inaccurate low interior velocities. Rotating flow phenomena only observed from a single profile often do not match expectations and intuition, and more detailed modeling is needed. Numerical simulations have been validated against experimental visualizations of both transient and stable-period flows.¹⁸ Dynamical systems and bifurcation theory have been used to clarify the transition scenario of the vortex dynamics. Xiao³⁰ studied the phenomenon of VB in an enclosed sealed cylinder by numerical simulation methods and explained the VB in the sealed cylinder with energy gradient theory. They used the energy gradient function K to explain the phenomenon of VB and found that the position of the local peak value of the energy gradient function K at the centerline was the first location where the flow lost its stability and subsequently caused a VB bubble. Carrión *et al.*³⁸ focused on the VB disappearance and explained the geometry of a cell of counter circulation—a vortex breakdown bubble (VBB) region. They explained that the convergence of the swirling flow to the axis reduced the pressure above the center of the stationary disk. Suction caused by the reduced pressure creates a VBB and attracts it closer to the disk. A VB emerges when the local minimum of the axial velocity at the rotating axis becomes negative. Recently, dynamic evolution of the position of the vortex structures was studied in plasma flow.³⁶ The induced velocity peak value and profile velocity height were analyzed to determine which plasma actuator has the strongest temporal aerodynamic efficiency. The physical properties of rotating flows are crucially dependent on their internal vortex structures.

However, due to the limitations of experimental technology, such as the velocity of the VB center being too small to be precisely measured and the vortex center being confused with the dye filament, leading to inaccurate low interior velocities, there are some unresolved problems: (1) quantitative study of the morphologies and trajectories of VBs has not been conducted; (2) how the aspect ratios and the Reynolds number (Re) affect the evolution of the VB morphology and propagation has rarely been discussed; (3) the reason that the pressure minimum and the center of VB do not coincide but are below the VB has not been determined.

In this work, we modeled the vortex pattern and trajectories of rotating water induced by a rotating lid in a closed sealed cylinder with the finite element method. We performed over 1900 simulations for four aspect ratios, $\lambda = 1.5, 2.0, 2.5,$ and 3.3 . We studied the axial length and propagation of VBs, and how one, two, and three VBs emerged, expanded, split, merged, shrank, and disappeared for four different aspect ratios as Re increased. Key related physical quantities, the velocity, pressure, and vorticity patterns, in the axisymmetric profile and the radial profile were investigated. Swirl theory was used to explain and analyze the mechanism of VB formation and propagation and uncover other as yet unknown fluid behaviors.

II. METHODS AND THEORY

The numerical technique of our study of rotating flow is similar to that used in our previous study.²⁵ Several software packages are available for vortex analysis and simulation in rotating flows. Among these packages, COMSOL Multiphysics is advantageous because of its

particular adaptability and compatibility when adding physics to an existing model. Moreover, COMSOL Multiphysics provides a complete and integrated environment for physics modeling and simulation as well as application design. This software is used to study vortices in axisymmetric flows.^{7,25} Furthermore, COMSOL Multiphysics can reduce the original axisymmetric three-dimensional (3D) geometry to a two-dimensional (2D) physics interface where the flow in the rotational direction is still included in the equations in rotating flows, which reduces the computing costs but includes all three velocity components. This method is suitable for physical quantities that have no or little change in the tangential direction; otherwise, some information may be lost.

The change of incompressible water was induced by a rotating disk in a sealed cylinder of height H and radius R in the COMSOL Multiphysics software. A stationary and axisymmetric flow can be described by the Navier–Stokes equations and the continuity equation²⁰

$$\rho \left(V_r \frac{\partial V_r}{\partial r} - \frac{V_\theta^2}{r} + V_z \frac{\partial V_r}{\partial z} \right) + \frac{\partial p}{\partial r} = \eta \left[\frac{1}{r} \frac{\partial}{\partial r} \left(r \frac{\partial V_r}{\partial r} \right) - \frac{V_r}{r^2} + \frac{\partial^2 V_r}{\partial z^2} \right] + F_r, \quad (1)$$

$$\rho \left(V_r \frac{\partial V_\theta}{\partial r} + \frac{V_r V_\theta}{r} + V_z \frac{\partial V_\theta}{\partial z} \right) = \eta \left[\frac{1}{r} \frac{\partial}{\partial r} \left(r \frac{\partial V_\theta}{\partial r} \right) - \frac{V_\theta}{r^2} + \frac{\partial^2 V_\theta}{\partial z^2} \right] + F_\theta, \quad (2)$$

$$\rho \left(V_r \frac{\partial V_z}{\partial r} + V_z \frac{\partial V_z}{\partial z} \right) + \frac{\partial p}{\partial z} = \eta \left[\frac{1}{r} \frac{\partial}{\partial r} \left(r \frac{\partial V_z}{\partial r} \right) + \frac{\partial^2 V_z}{\partial z^2} \right] + F_z, \quad (3)$$

$$\nabla \cdot \vec{V} = \frac{1}{r} \frac{\partial}{\partial r} (r V_r) + \frac{\partial V_z}{\partial z} = 0, \quad (4)$$

where $\vec{V} = (V_r, V_\theta, V_z)$ denotes the velocity (m/s), V_r denotes the radial velocity, V_θ denotes the swirl/tangential velocity, V_z denotes the axial velocity, ρ denotes the density (kg/m^3), η denotes the dynamic viscosity (Pa s), p denotes the pressure (Pa), and $\vec{F} = (F_r, F_\theta, F_z)$ denotes the volumetric force.

We use the theory of swirl decay^{60,61} to analyze the physical mechanism of the VB. The swirl and axial velocities in a sealed cylinder can be described as follows:

$$V_\theta = F(r) \exp(-\gamma z), \quad V_z = W(r) \exp(-\gamma z), \quad (5)$$

where γ is a decay rate, $0 < \gamma < 1$. Equation (5) is valid internally, not near the boundaries.

Let us introduce the following dimensionless variables:^{15,16}

$$\begin{aligned} V'_r &= V_r/\omega R, & V'_\theta &= V_\theta/\omega R, & V'_z &= V_z/\omega R, & r' &= r/R, \\ z' &= z/R, & p' &= p/(\rho\omega^2 R^2), & F'_r &= F_r/(\rho\omega^2 R), & & \\ F'_\theta &= F_\theta/(\rho\omega^2 R), & F'_z &= F_z/(\rho\omega^2 R), & \zeta' &= \zeta/\omega, & & \end{aligned} \quad (6)$$

then $V'_r, V'_\theta, V'_z, r', z', p', F'_r, F'_\theta, F'_z$ satisfy

$$\begin{aligned} & \left(V'_r \frac{\partial V'_r}{\partial r'} - \frac{V'^2_\theta}{r'} + V'_z \frac{\partial V'_r}{\partial z'} \right) + \frac{\partial p'}{\partial r'} \\ &= \frac{1}{Re} \left[\frac{1}{r'} \frac{\partial}{\partial r'} \left(r' \frac{\partial V'_r}{\partial r'} \right) - \frac{V'_r}{r'^2} + \frac{\partial^2 V'_r}{\partial z'^2} \right] + F'_r, \end{aligned} \quad (7)$$

$$\left(V'_r \frac{\partial V'_\theta}{\partial r'} + \frac{V'_r V'_\theta}{r'} + V'_z \frac{\partial V'_\theta}{\partial z'} \right) = \frac{1}{Re} \left[\frac{1}{r'} \frac{\partial}{\partial r'} \left(r' \frac{\partial V'_\theta}{\partial r'} \right) - \frac{V'_\theta}{r'^2} + \frac{\partial^2 V'_\theta}{\partial z'^2} \right] + F'_\theta, \quad (8)$$

$$\left(V'_r \frac{\partial V'_z}{\partial r'} + V'_z \frac{\partial V'_r}{\partial z'} \right) + \frac{\partial p'}{\partial z'} = \frac{1}{Re} \left[\frac{1}{r'} \frac{\partial}{\partial r'} \left(r' \frac{\partial V'_z}{\partial r'} \right) + \frac{\partial^2 V'_z}{\partial z'^2} \right] + F'_z, \tag{9}$$

$$\nabla' \cdot \vec{V}' = \frac{1}{r'} \frac{\partial}{\partial r'} (r' V'_r) + \frac{\partial V'_z}{\partial z'} = 0. \tag{10}$$

The dimensionless method^{15,16} is a common way to study physical problems with mathematical tools, where parameters can be reduced and certain mathematical problems simplified by choosing appropriate transformations. In our simulations, the volumetric force components F'_r , F'_θ , and F'_z were set to zero. Rotating flows were initiated by the upper rotating disk with angular velocity ω . The sealed cylinder was described with the aspect ratio $\lambda = H/R$. The Reynolds number, which characterizes the relative importance of the inertial and viscous forces, was defined as $Re = \omega R^2/\nu$, where $\nu = \eta/\rho$ is the kinematic viscosity.^{7,17} The angular velocity ω and aspect ratio λ were adjustable, and the radius R was 17.5 mm. The density of water was $1.0 \times 10^3 \text{ kg/m}^3$, and the dynamic viscosity was $1.0 \times 10^{-3} \text{ Pa}\cdot\text{s}$. Because the flow showed a negligible departure from axisymmetry until into the unsteady-flow domain,¹⁷ we reduced the original 3D geometry to 2D. We set the top boundary as a sliding wall ($0 \leq r' < 1, z = \lambda$),¹⁵

$$V'_r = V'_z = 0, \quad V'_\theta = r', \tag{11}$$

and the sidewall ($0 \leq z' < \lambda, r' = 1$) and bottom boundary of the cylinder ($0 \leq r' \leq 1, z' = 0$) as non-slip walls

$$V'_r = V'_\theta = V'_z = 0, \tag{12}$$

and the rotation axis ($0 \leq z' < \lambda, r' = 0$) as axisymmetric boundary

$$V'_r = V'_\theta = \frac{\partial V'_z}{\partial r'} = 0. \tag{13}$$

We implemented the simulations by utilizing the finite element approach based on the commercial software COMSOL Multiphysics. The rotating velocity change was realized by a parameter auxiliary sweep, and large amounts of data were analyzed using Python.

III. RESULTS AND DISCUSSION

The physical properties of rotating flows are crucially dependent on their internal VB patterns. We performed over 1900 simulations for four aspect ratios, $\lambda = 1.5, 2.0, 2.5,$ and 3.3 . The major simulation parameters of the VB are summarized in Table I, where N is the number of simulations.

The basic numerical simulation of rotating flows in a sealed cylinder, schematic view of the sealed cylinder, and the streamlines and

TABLE I. Major simulation parameters of internal vortex breakdown (VB) in sealed cylinders.

Case	R (m)	H (m)	$\lambda = H/R$	$Re = \omega R^2/\nu$	Re interval	N
1	0.0175	0.02625	1.5	800–6000	10	521
2	0.0175	0.03500	2.0	800–6000	10	521
3	0.0175	0.04375	2.5	1700–6000	10	431
4	0.0175	0.05775	3.3	2500–7100	10	461

velocity components at $Re = 800$ are shown in Fig. 1. Water filled the sealed cylinder, and the aspect ratio was defined as $\lambda = H/R$ [see Fig. 1(a)]. There was meridional circulation induced by the disk rotation [Fig. 1(b)]: water moved away from the rotating disk along the sidewall, converged to the axis near the stationary disk, and moved back to the rotating disk near the axis, forming a centrifugal circulation cell. The swirl velocity [Fig. 1(d)] was much larger than the radial velocity [Fig. 1(c)] and the axial velocity [Fig. 1(e)]. Compared with the swirl and axial velocities, the radial velocity was negligible. According to the cyclostrophic balance, the centrifugal force, $\rho V_\theta^2/r$, induced a radial gradient of pressure $\partial p/\partial r$, namely, $\rho V_\theta^2/r = \partial p/\partial r$, where ρ is the water density, V_θ is the swirl velocity, and r is the distance from the rotation axis. The pressure near the rotation axis is smaller than that in the periphery. The stronger the swirl is, the larger the pressure reduction is. The axial velocity was positive in the hour-glass structure domain, which means that in this domain, the water flowed upward, and it flowed downward in other areas [Fig. 1(e)]. In this study, we focused on the internal VB morphology and propagation characteristics around the sealed cylinder axis for multiple aspect ratios at large values of Re .

A. Morphology of separated vortex rings (VBs) for four aspect ratios

The morphology of vortex breakdown (VB) was a pair of counter-centrifugal circulation cells. Figure 2 shows the patterns of this rotating flow in the axisymmetric profile at a few increasing characteristic values of Re , illustrating how a VB emerged, expanded, contracted, and disappeared when the aspect ratio $\lambda = 1.5$. Water rotating around the sealed cylinder axis moved toward to the rotating disk, while water near the bottom stationary disk moved toward the sealed cylinder axis. At $Re = 1050$, the streamlines near the axis formed a bulge, which expanded along the radial direction. At about $Re = 1080$, a VB began appearing in the bulge domain, and the VB began expanding and grew near the axis. The VB almost grew to the largest value at $Re = 1400$; then, it slowly decayed and disappeared at $Re = 2000$. In addition, the height of the VB center descended quickly initially and then slowly with increasing Re .

The Re dependence of multiple VBs for $\lambda = 2.0, 2.5,$ and 3.3 are shown in Figs. 3–5. For $\lambda = 2.0$, two VBs emerged and disappeared at the axis in the range of $Re = 1400$ – 3020 , as shown in Fig. 3. At $Re = 1400$, the streamlines near the axis began forming a bulge, and this bulge expanded along the radial direction. At $Re = 1500$, a VB began to appear in the bulge domain near the axis, and a new bulge appeared above the first VB. The first VB began developing and grew near the axis, and the first VB moved toward to the bottom stationary disk. The bulge above the VB developed and grew to the second VB at $Re \approx 1850$; then, it slowly decayed and disappeared at $Re = 2500$, while the first VB still slowly decayed and disappeared at $Re = 3020$. There were two VBs in the rotating fluids in the range of $Re \approx 1850$ to 2200 . The first VB appeared at a lower Re than the second VB and disappeared at a higher Re than the second VB.

For $\lambda = 2.5$, streamline patterns at a few increasing characteristic values of $Re = 1700$ – 6000 are shown in Fig. 4. At $Re = 1700$, the streamlines near the axis formed two bulges, and these bulges expanded along the radial direction. In the range of $Re = 1970$ – 2100 , a VB began appearing in the bulge domain near the axis, and another bulge developed into a new VB. The two VBs began developing and

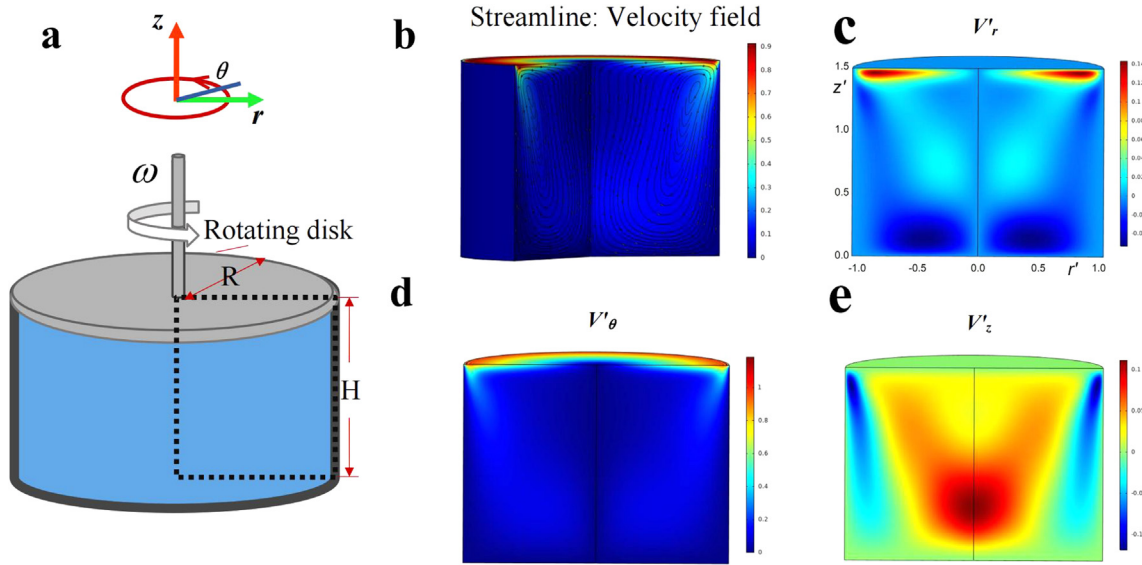


FIG. 1. Rotating flows in a sealed cylinder. (a) Schematic view of the sealed cylinder, with water filling the cylinder. (b)–(e), Streamlines, radial velocity, swirl velocity, and axial velocity in the $r' - z'$ plane at the sheared steady state with $Re = 800$ and $\lambda = 1.5$.

grew near the axis, and the two centers of the VBs moved toward the bottom stationary disk with increasing Re . The top bulge was developing and grew to the second VB at $Re = 2300$ and then slowly decayed. The upper VB disappeared at $Re = 3800$, while the lower VB still slowly decayed and disappeared at $Re = 6000$. There were two VBs in the rotating fluids in the range of $Re = 1970 - 3600$. The first VB

appeared first and disappeared last, while the second VB appeared last and disappeared first in the range of $Re = 3600 - 6000$.

For $\lambda = 3.3$, three VBs emerged and disappeared in the range of $Re = 2700 - 7100$, as shown in Fig. 5. At $Re = 2700$, the streamlines near the axis formed two bulges; the lower lump was round, and the upper lump was slender. A VB first appeared in the lower lump domain

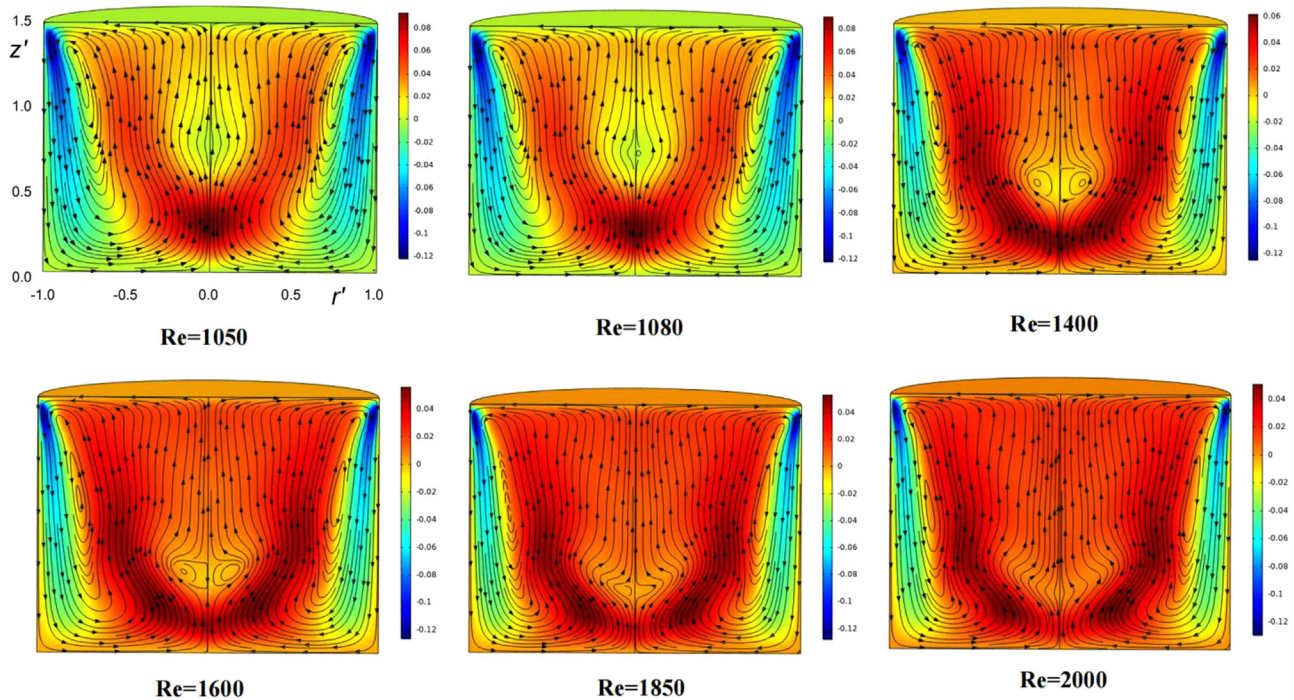


FIG. 2. Development of vortex breakdown (VB) at a few characteristic values of Re for $\lambda = 1.5$. Black lines represent streamlines.

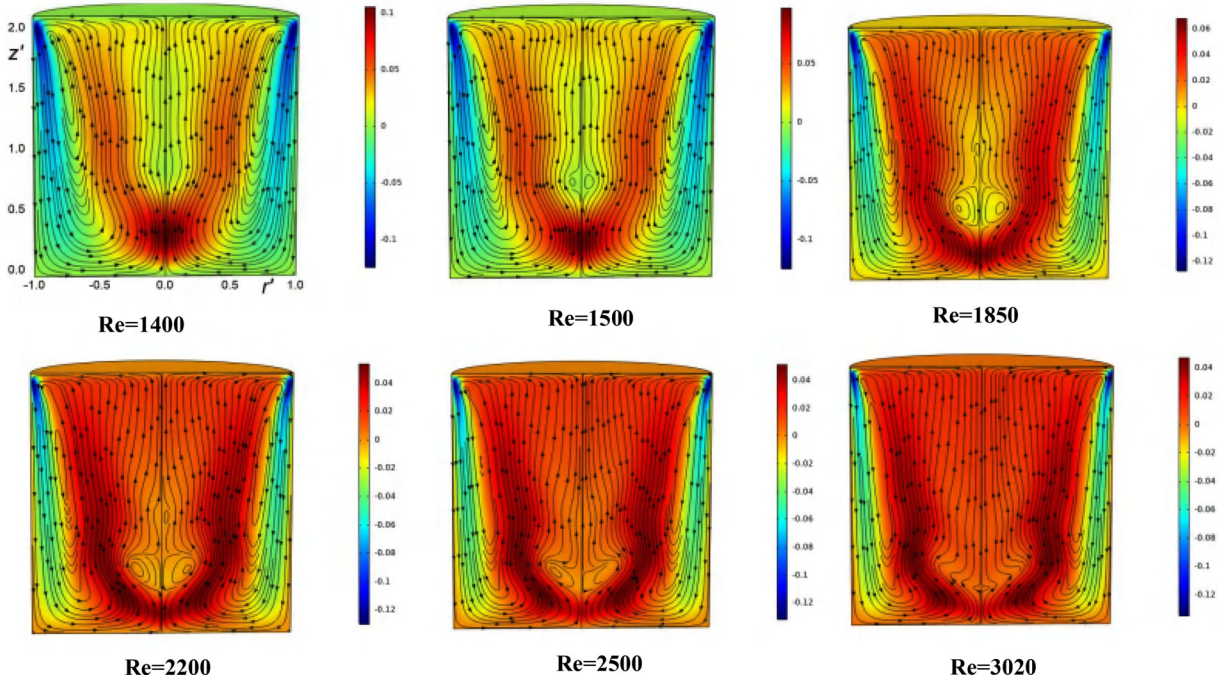


FIG. 3. Evolution of two VBs at a few increasing characteristic values of Re for $\lambda = 2.0$. Black lines represent streamlines.

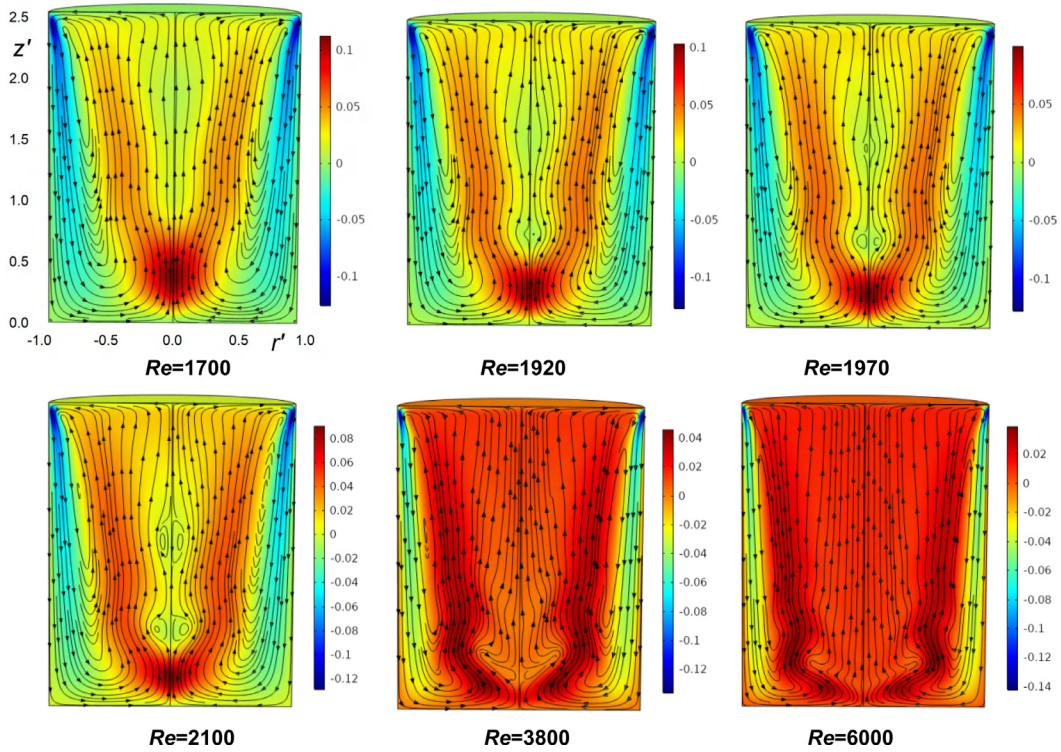


FIG. 4. Development of two VBs at a few characteristic values of Re for $\lambda = 2.5$. Black lines represent streamlines.

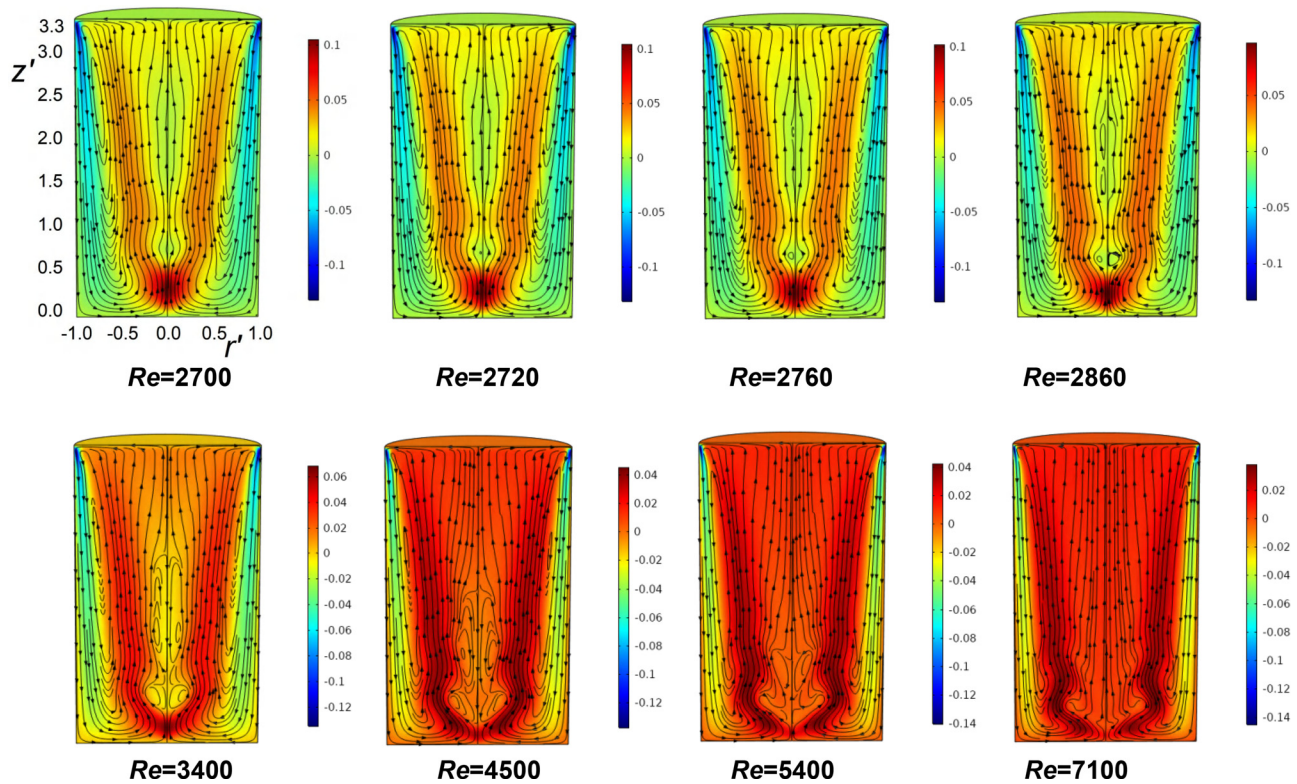


FIG. 5. Development of three VBs at a few characteristic values of Re for $\lambda = 3.3$. Black lines represent streamlines.

at $Re = 2720$, and the symmetry of this VB was slightly weaker than that for other aspect ratios. At $Re = 2760$, in the upper lump domain, a new VB also appeared close to the rotating disk. In the range of $Re = 2860$ – 3400 , three VBs appeared near the sealed cylinder axis, one in the lower lump domain and two in the upper lump domain. From $Re = 3400$ to 4500 , the two VBs merged together, forming a large VB, and this VB moved downward to the VB in the lower lump domain. The upper VB slowly decayed and disappeared in the range of $Re = 4500$ – 7100 . The upper VB disappeared at lower Re than the lower VB. When there were multiple VBs, the first VB appeared first and disappeared last, while the second VB appeared last and disappeared first. If the two VBs were in the same lump domain, they merged together, forming a large VB as Re increased. There are minor differences in the streamlines shown in Figs. 2–5, which are also present in the experiment.⁵⁶ We performed simulations that show that the mesh sizes fine, finer, and extra fine have almost no effect on the results, and the mesh distribution in the near-axis region is nearly uniform, so the mesh is not the main cause of minor differences in the results. The Reynolds number and the seal cylinder structure may be the main factors causing the minor differences.

B. Key flow characteristics along the axis, axial velocity, pressure, and vorticity patterns in axisymmetric profile

Because the VB centers were located at the axis, it was necessary to study the distribution of the key flow characteristics along the axis

and the key physical quantities that caused the VBs. Figure 6 shows the results at $Re = 800$ – 6000 with intervals of 10 for $\lambda = 1.5$. Figures 6(a)–6(c) show the key flow characteristics along the axis. The z' profiles of the axial velocity at the $r' = 0$ are shown in Fig. 6(a). As Re increased, the peak values of axial velocities decreased as Re increased, and the positions of z' corresponding to the peak value gradually decreased and moved toward the stationary disk. The V'_z local minimum first decreased until $Re = 1400$ and then increased gradually, and the z' -coordinate corresponding to the V'_z local minimum approached the stationary disk. The inset figure shows that some minimum values of V'_z at $Re = 1000, 1050, 1950,$ and 2000 were positive, and no VB was generated in the rotating water. The minimum values were negative in the approximate range of $1050 < Re < 1950$ where the VB existed. The change of a fluid depends on the pressure. The distributions of the pressure (p') at the axis at a few characteristic Re values are shown in Fig. 6(b). As Re increased, the pressure (p') at the axis at $r' = 0$ increased. The dotted curve showed that the pressure minimum (p'_{\min}) value increased and the location shifted toward the stationary disk caused by the converging flow to the axis vicinity as Re increased. Figure 6(c) shows the vorticity magnitude ζ' at the axis at a few characteristic Re values. The curves reveal that the vorticity magnitude ζ' at the axis did not monotonically decay from the rotating disk toward the stationary disk. There was a local maximum of the vorticity near $z' = 0.343$ at $Re = 800$. As Re increased, this local peak value increased and then decreased during the simultaneous movement of the ζ' maximum toward the stationary disk vicinity. The intensification of the swirl near the stationary disk center was

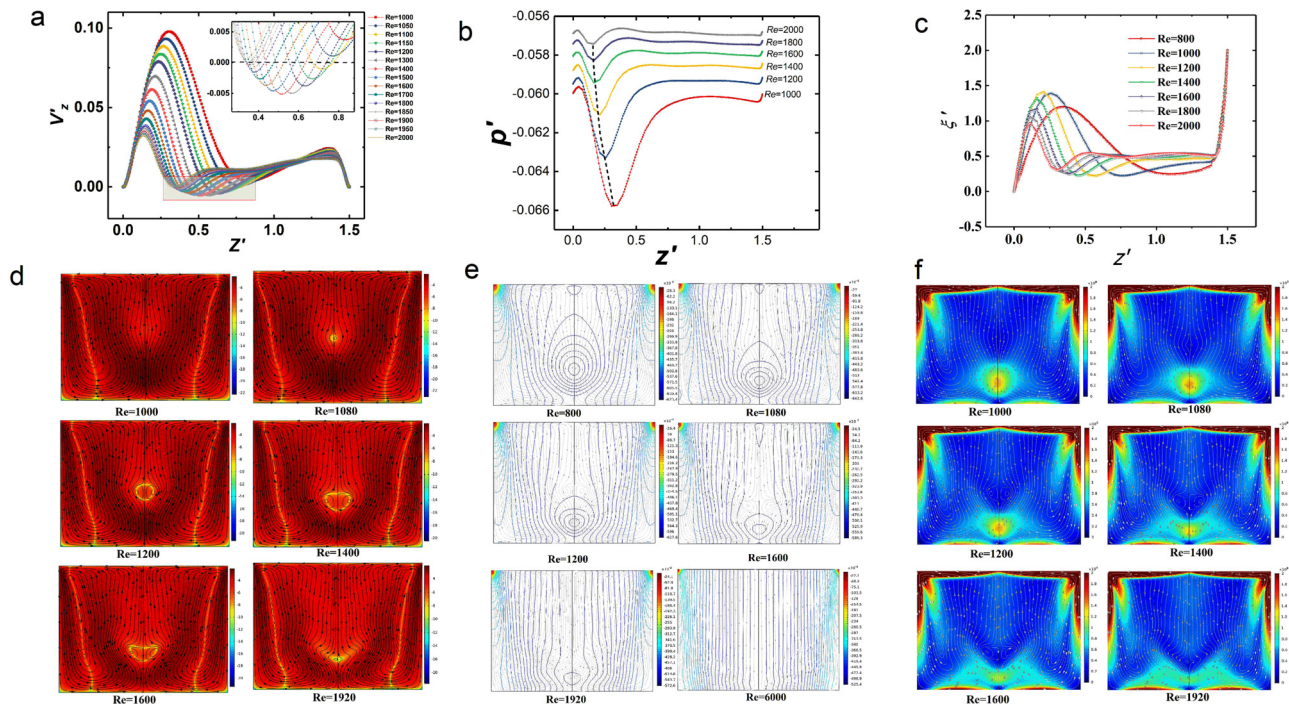


FIG. 6. Distributions of (a) axial velocity V_z' , (b) pressure, and (c) vorticity magnitude at $r' = 0$ for a few characteristic values of Re and $\lambda = 1.5$. (d) Streamline patterns of $\log(|V_z'|)$, (e) contours of constant pressure, and (f) vorticity magnitude.

caused by angular momentum from the fluid convergence to the axis vicinity.

Figures 6(d)–6(f) show the distribution of the streamlines, axial velocity, pressure, and vorticity for $\lambda = 1.5$. Because the natural logarithm can magnify the value near zero, we plotted the axial velocity in the form $\log(|V_z'|)$ and the corresponding streamlines patterns in Fig. 6(d). The yellow areas represent the local velocity $|V_z'|$ being very close to or equal to zero, while the red areas represent the velocity $|V_z'|$ being greater than zero. Two yellow curves pass through the slender vortex near the edge in the sealed cylinder. As Re increased to 1080, a VB emerged when the local minimum of the axial velocity $\log(|V_z'|)$ formed a closed circle, a yellow circle at the axis. Both the VB and the yellow circle expanded as Re increased to 1400, then shrank until $Re = 1920$ and disappeared when $Re > 1920$. Whether the local minimum value of $\log(|V_z'|)$ near the axis formed a closed circle was the precisely condition for judging the appearance and disappearance of the VB. The result showed a distinct feature that the location of the VB shifted along the axis from the middle of the axis vicinity at $Re = 1080$ to the stationary disk vicinity at $Re = 1920$.

Figure 6(e) shows contours of constant pressure (rainbow lines) and streamlines (gray lines) for the same increasing characteristic values of Re . There was a low-pressure area at the axis because of the convergence of the swirling flow to the axis above the center of the stationary disk, and the location of the minimum-pressure domain shifted toward the stationary disk vicinity as Re increased. The patterns showed that the suction of the minimum-pressure domain generated a VB and attracted it to the stationary disk in the range of $Re = 1080$ –1920. As Re increased above 1600, the pressure gradient of

the low-pressure region decreased, and the contours of constant pressure tended to become parallel to the axis. The diminishing of the axial gradient of the pressure and the weakening of the suction led to the disappearance of the VB when $Re > 1920$.

Figure 6(f) shows the vorticity magnitude and streamlines in the axisymmetric profile at a few characteristic values in the range of $Re = 1000$ –1920. It shows that a local maximum of the swirl vorticity domain appeared close to the axis near the stationary disk, and the value of the maximum of the swirl vorticity increased as Re increased in the range of 1000–1400. That location of the vorticity maximum domain shifted toward the stationary disk vicinity. The reason was that water flow convergence transported the angular momentum to the axis vicinity. When $Re > 1400$, this domain expanded to the sidewall and the maximum decreased. As Re increased, the near-axis flow convergence became weak because more water continuously descending near the sidewall turned upward when it reached the stationary disk vicinity before approaching the axis vicinity. This part of the water flowed upward due to the growing centrifugal force produced by the significant increase in vorticity near the stationary disk.

C. Swirl velocity and radial pressure gradient patterns in radial profiles

To further uncover the physical mechanism of fluid convergence, the swirl velocity and radial pressure gradient were studied in the radial profiles at various distances h' for a stationary disk with $Re = 1200$ for $\lambda = 1.5$ (Fig. 7). As shown in Fig. 7(a), the maximum of the swirl velocity decreased gradually as h' decreased. The top three plots show that the swirl velocity increased almost linearly, with slight

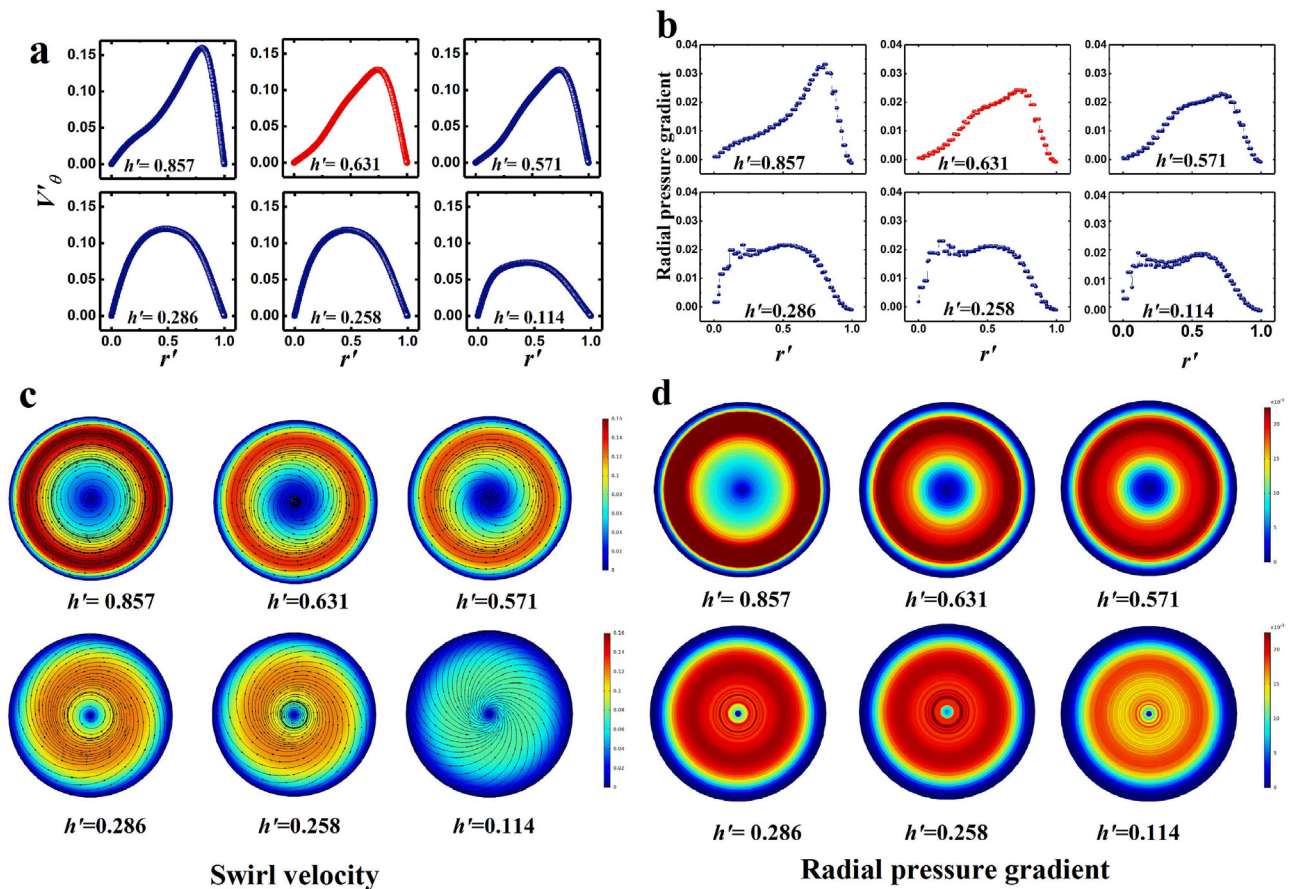


FIG. 7. Radial distribution and internal three-dimensional (3D) flow patterns of swirl velocity and variation trends of radial pressure gradient at various distances h' relative to the stationary disk at $Re = 1200$ and $\lambda = 1.5$. (a) Radial distribution of swirl velocity and (b) variation trends of radial pressure gradient with increasing depth. (c) Internal 3D swirl velocity and (d) radial pressure gradient patterns in the radial profiles.

fluctuations in the r' range 0–0.8, then dropped rapidly to zero at the edge. The bottom three plots showed that the velocity curve was arched and the maximum value was near $r' = 0.514$. There were rich internal 3D flow structures at different h' values [Fig. 7(c)]. At the same time, the high-speed belt near the edge gradually diffused to the middle region, as shown in the red and yellow regions. Some water flowed and diffused to the edge, some flowed and converged to the axis, and some converged to the middle ring belt. A VB appeared at $h' = 0.631$, and the minimum pressure on the rotating axis was at $h' = 0.258$. For both plots, there were relatively dense areas of streamlines on the rotating axis. This demonstrated that there was a significant difference of the internal microstructures of the rotating flows.

The curves in Fig. 7(b) show the fluctuation and variation trends of the radial pressure gradient with decreasing height. The center of the VB was located at $h' = 0.631$, and there was a gentle and relatively small pressure gradient area (blue area), which was suitable for the stability of the VB. As the height descended, the fluctuation of the pressure gradient near the rotating axis became more and more evident, and the pressure gradient changed in a step shape. The fluctuation of the pressure gradient and the step-like change may have been the main factors causing the significant differences of the internal

microstructures of the rotating flows. The radial pressure gradient in the radial profiles was analyzed to explain the abundant internal microstructures [Fig. 7(d)]. The pressure gradient did not increase all the way but fluctuated along the radial direction, forming a circular band of pressure gradients. With the increase in the depth, the ring band with a large pressure gradient near the edge gradually drew closer to the center, and the pressure gradient fluctuated during the process of drawing closer. The area of a small pressure gradient near the rotating axis gradually shrank, which meant that the pressure gradient near the axis became larger and larger. The fluctuation of the pressure gradient may have been the main cause of the VB patterns.

D. Axial length of VBs varied with increasing Re under different structures

To further quantify the morphological evolution of the VB with increasing Re , we quantitatively studied the axial length of the VB. The axial length of the VB was described by the spacing between the upstream and downstream streamline stationary points at the axis of rotation where the VB occurred.⁷ The VB axial lengths of different structures were calculated using Python. Figure 8 shows that the length

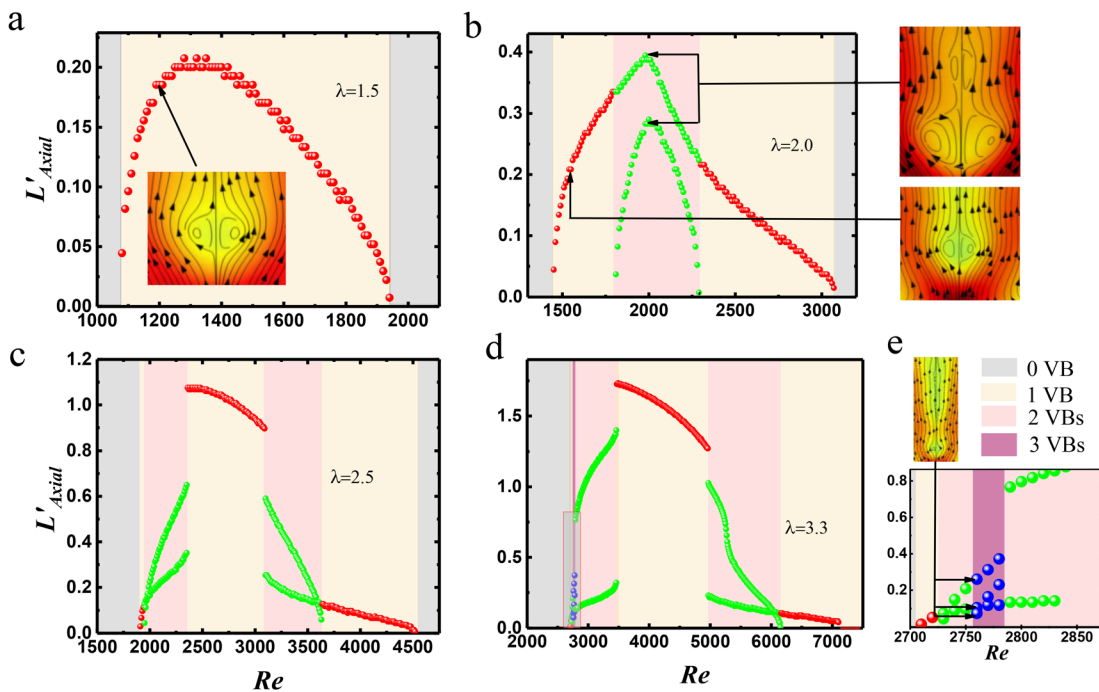


FIG. 8. Paraxial streamwise length of VBs changed continuously with increasing Re for four structures. (a) One VB emerged (see the inset figure), expanded, shrank, and disappeared with $\lambda = 1.5$. The inset figure shows the steady VB at $Re = 1200$. (b) For $\lambda = 2.0$, one steady VB evolved into two VBs, then merged into one VB, and finally disappeared. The right figures show one stable VB (bottom) and two stable VBs (top). (c) One small VB quickly split into two VBs, then merged into one larger VB. This VB again split into two VBs, then merged into one VB, and finally disappeared ($\lambda = 2.5$). (d) One small VB quickly split into two VBs, split into three VBs, then merged into two larger VBs. The two larger VBs merged into one larger VB, again split into two small VBs, then merged into one VB, and finally disappeared ($\lambda = 3.3$). (e) Three stable VBs, where different background colors represent different VB intervals (top). The partial enlargement of figure (d) shows the complex evolution of the VBs (bottom).

of the VB varied continuously with increasing Re for the four structures. For $\lambda = 1.5$ [Fig. 8(a)], only one stable VB appeared in the range of $Re = 1073\text{--}1941$. A VB appeared around $Re = 1100$, expanded to a maximum around $Re = 1370$, and then slowly shrank and finally disappeared. The specific results show the evolution of the number of VBs for $\lambda = 1.5$ was as follows: $0 \rightarrow 1 \rightarrow 0$.

As Re increased, up to two VBs appeared in the rotating fluid when $\lambda = 2.0$ and 2.5 [Figs. 8(b) and 8(c)]. For $\lambda = 2.0$, a stable VB appeared and evolved into two VBs, then merged into one VB, and finally disappeared with increasing Re . The evolution of the number of VBs was as follows: $0 \rightarrow 1 \rightarrow 2 \rightarrow 1 \rightarrow 0$. For $\lambda = 2.5$, as Re increased, a small VB was created and quickly split into two VBs, which then merged into a larger VB; this VB split again into two VBs, which then merged into one VB and finally disappeared. The evolution of the VB number was as follows: $0 \rightarrow 1 \rightarrow 2 \rightarrow 1 \rightarrow 2 \rightarrow 1 \rightarrow 0$. Both generated at most two VBs for $\lambda = 2.0$ and 2.5 . The larger the aspect ratio was, the more complex the evolution of the VB was, and after growing, splitting, and merging, the VBs split and merged again and eventually disappeared.

Figure 8(d) shows that the VB at $\lambda = 3.3$ seemed to evolve in the same way as that at $\lambda = 2.5$. However, the evolution of the VB was made more complex and mysterious by zooming in on the image [Fig. 8(e)] showing the appearance of three VBs in the range of $Re = 2750\text{--}2800$. It began with one VB, split into two VBs, and then split into three VBs. These three VBs rapidly merged into two large

VBs, which merged into one largest VB. This largest VB split again into two VBs, which then merged into one VB, decayed, and finally disappeared. The evolution of the number of VBs was as follows: $0 \rightarrow 1 \rightarrow 2 \rightarrow 3 \rightarrow 2 \rightarrow 1 \rightarrow 2 \rightarrow 1 \rightarrow 0$.

The results showed that the VB axial dimension varied nonlinearly with the increase in Re . With the increase in the structure factor, the nonlinear phenomenon of the VB axial dimension variation became more complicated, not only in terms of the variation of the VB number but also VB generation, splitting, merging, secondary splitting, secondary merging, and even tertiary splitting. The maximum axial dimension of the VB also increased with the increase in the structure factor.

E. Stair-step effect of axial velocity, pressure, and vorticity on VB trajectories

In order to fully understand the mechanism of VB generation, especially the change mechanism of VBs for different aspect ratios, we calculated the extreme value distributions of the axial velocity, pressure, and vorticity at $r' = 0$. The specific point locations associated with the VB for four different aspect ratios were obtained, as shown in Figs. 9(a)–9(f). We processed more than 5800 raw data curves of the axial velocity, pressure, and vorticity with Python. The upper three figures show the distribution of the extreme Re values for the axial velocity, pressure, and vorticity. The lower figures show the locations corresponding to the extreme values.

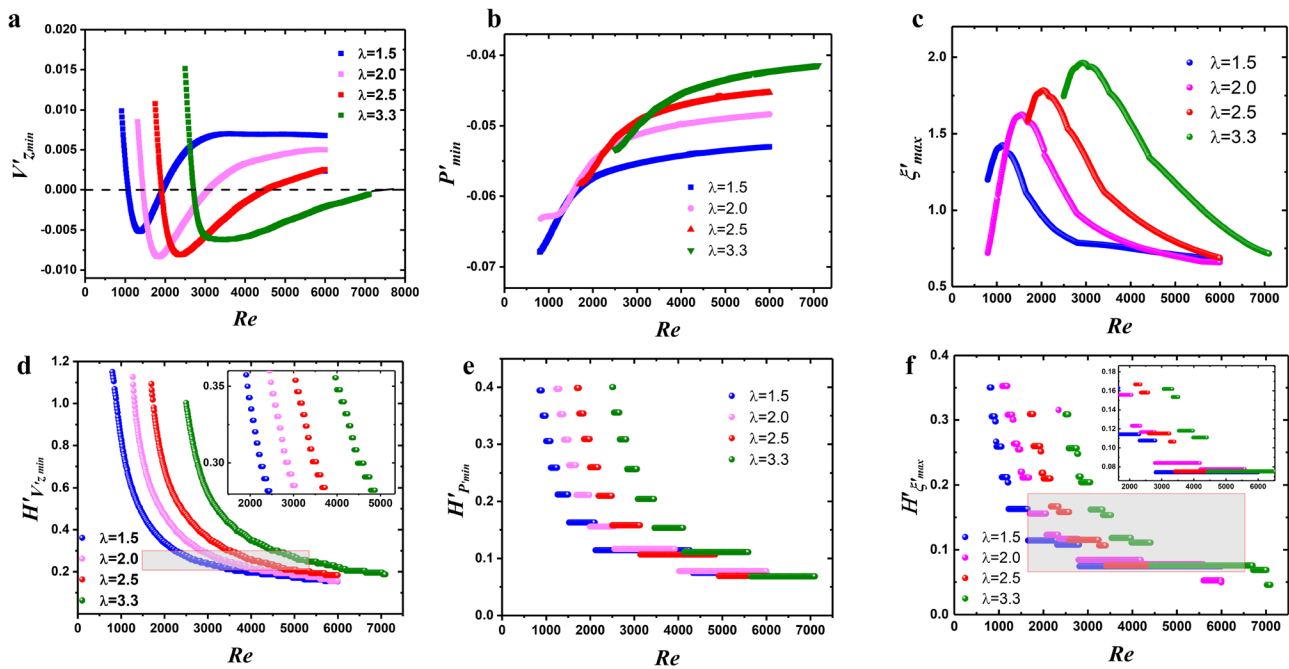


FIG. 9. Extreme value distributions of the axial velocity, pressure, and vorticity at $r' = 0$ and the particular point locations of the VB for four different aspect ratios. Extreme value distributions of (a) axial velocity, (b) pressure, and (c) vorticity for different values of Re . (d)–(f) Corresponding locations of the extreme values.

Figure 9(a) depicts the dependence of the minimum value of the axial velocity V'_{zmin} on Re in the rotation axis. V'_{zmin} decreased rapidly and then increased gradually as Re increased. The VB appeared when $V'_{zmin} < 0$; the VB continued to grow until V'_{zmin} dropped to the curve minimum, where the VB expanded to a maximum. Then, V'_{zmin} began to increase and the VB began to contract until it disappeared when $V'_{zmin} > 0$. The VB judgment criterion was that if $V'_{zmin} < 0$, the VB existed; if $V'_{zmin} > 0$, the VB did not exist. The trough of the $V'_{zmin} - Re$ curve revealed that the VB expanded to the maximum.

The exact Re value corresponding to the appearance and disappearance of the VB was determined by using an interpolation method based on the VB evolution judgment criteria, as shown in Table II. N_{maxVB} is the maximum number of VBs, Re_A is the critical Re value for the first appearance of a VB, Re_M is the critical Re value for the expansion of a VB to its maximum, Re_D is the critical Re value for the disappearance of a VB, and ΔRe_{VB} is the existence of the Re interval of a VB. For $\lambda = 1.5$, a VB appeared, expanded, contracted, and disappeared in the range of $Re = 1073$ – 1941 . For $\lambda = 2.0$ and 2.5 , at most

two VBs were generated, and the ranges of the corresponding Re for which the VBs existed were 1444 – 3088 and 1906 – 4539 . For $\lambda = 3.3$, up to three VBs occurred, developed, contracted, and disappeared in the range of $Re = 2707$ – 7539 . As the aspect ratio λ increased, the Re value corresponding to the first occurrence in the VB increased, expanding to a maximum at higher Re values, and the Re interval in which the VB existed was larger.

The variation in the minimum pressure P'_{min} and maximum vorticity ξ'_{max} at $r' = 0$ for different aspect ratios is shown in Figs. 9(b) and 9(c). The curves in Fig. 9(b) show that the minimum P'_{min} increased monotonically as Re increased for all the aspect ratios. The larger the aspect ratio λ was, the larger the rate of increase in P'_{min} was at $r' = 0$. P'_{min} increased monotonically with increasing Re , regardless of whether VB appeared or disappeared. For all λ , the rate of increase in the pressure minimum at $r' = 0$ was divided into two stages, starting fast and growing at a similar rate, and then growing slowly as Re increased.

Under the VB, there was a local vorticity maximum region on the axis near the stationary disk. From Fig. 9(c), it can be seen that the local vorticity maximum ξ'_{max} on the axis changed considerably, with ξ'_{max} first increasing rapidly to a certain value, then decreasing rapidly, and finally decreasing gradually. At lower Re , the convergence effect was stronger than the rotation effect, and the converging flow transported the angular momentum near the axial direction, which enhanced the fluid rotation and led to a gradual increase in ξ'_{max} . When Re was further increased, the convergence effect balanced the rotation effect, and ξ'_{max} reached the maximum value. As Re increased, the convergence effect was weaker than the rotation effect, and more and more of the water descending near the sidewall flipped upward

TABLE II. Precise Re range of VB appearance, maximum, and disappearance.

Case	R (m)	H (m)	$\lambda = h'$	N_{maxVB}	Re_A	Re_M	Re_D	ΔRe_{VB}
1	0.0175	0.02625	1.5	1	1073	1410	1941	868
2	0.0175	0.03500	2.0	2	1444	1930	3088	1644
3	0.0175	0.04375	2.5	2	1906	2490	4539	2633
4	0.0175	0.05775	3.3	3	2707	4110	7539	4822

when it approached the stationary disk before approaching the axis, which led to a rapid decrease in ζ'_{\max} and an expansion of the local vorticity to an extremely large domain away from the axis. When Re increased to a larger value, the centrifugal cycle accelerated so that the angular velocity of water near the stationary disk increased and ζ'_{\max} began to decrease slowly.

Figure 9(d) shows the dependence of the V'_{zmin} positions, $H'_{V'_{zmin}}$, on Re for $\lambda = 1.5, 2.0, 2.5,$ and 3.3 . The curves show that $H'_{V'_{zmin}}$ decreased exponentially, first fast and then slow. For small Re , a small vorticity could not match the meridional change because the vortex flow decayed rapidly from the rotating disk. As Re increased, the enhanced sidewall effect caused a slow decrease in the V'_{zmin} position. With a further increase in Re , the increase in the centrifugal force led to radial expansion of the local maximum vorticity region, which caused the position of V'_{zmin} to decrease more slowly. The results showed that the decay rate of the position decreased slightly near the stationary disk as λ increased. This was because the higher H' was, the longer the flow descent path near the sidewall became. A larger Re was needed for the convergence effect to become dominant. The inset is an enlargement, which shows the interesting feature that the position of V'_{zmin} decreased in steps as Re increased. It is an interesting feature that the location of V'_{zmin} showed a stepwise descent with increasing Re . If $V'_{zmin} < 0$, the position of the VB can be represented by the V'_{zmin} position. The VB moved in a stepwise manner toward the stationary disk with a step height of $\Delta H' = 0.00743$. When the VB moved to a certain position, it needed gather sufficient energy from the converging flow to overcome the energy barrier in order to approach the stationary disk.

The minimum pressure domain suction drove the VB in a stepwise manner toward the stationary disk as Re increased. We studied the dependence of the p'_{min} position, $H'_{p'_{min}}$, on Re for $\lambda = 1.5, 2.0, 2.5,$ and 3.3 , as shown in Fig. 9(e). This shows that position of p'_{min} decreased exponentially, first faster and then slower. The step effect was significant in the movement of the pressure minimum toward the vicinity of the stationary disk. For the same λ , the position of p'_{min} was lower than that of V'_{zmin} , closer to the stationary disk. The step height $\Delta H' \approx 0.0457$, and the step width ΔRe widened as Re increased. The step width ΔRe can correspond to the energy potential to some extent. The closer the pressure minimum was to the fixed disk, the larger the step width ΔRe was, and the higher the energy potential barrier was that the fluid needed to overcome.

According to the cyclostrophic balance, the radial pressure gradient was caused by the centrifugal force. That is, the stronger the fluid rotation was, the greater the pressure drop became. Figure 9(c) shows the local vorticity maximum domain ζ'_{\max} position distribution. The position of ζ'_{\max} decreased exponentially, first faster and then slower. For the same λ , the ζ'_{\max} position was lower than that of V'_{zmin} , similar to the p'_{min} position, and it stopped near the stationary disk. The stair-step effect was more pronounced during the movement of the vortex maximum position toward the vicinity of the stationary disk. However, the step change was relatively complex compared to the changes in the velocity and pressure. The step change shown in the illustration was a combination of two-step changes: a primary step change and a secondary step change. For the primary step change, the step height was $\Delta H'_M$ and the step width was ΔRe_M . For the secondary step change, the step height was $\Delta H'_S$, and the width was ΔRe_S . The step height of the primary step change $\Delta H'_M \approx 0.0457$, which was the

same as that of the $H'_{p'_{min}}$ change. The secondary step height $\Delta H'_S$ was about 0.00686, which was slightly smaller than that of the $H'_{V'_{zmin}}$ change. ΔRe_M and ΔRe_S increased as the maximum position of the local vorticity moved toward the stationary disk to overcome a larger energy potential. The secondary step change may have been caused by the competition of flow convergence and rotation. The primary step change of the vorticity maximum may have been the main factor causing the step change of the pressure minimum, and the secondary change of the vorticity maximum caused the axial velocity minimum step change. This could also explain why the center of the pressure minimum was below the VB. The major step change of the vorticity maximum caused a relatively large drop in the location of the pressure minimum, which dropped lower than the center of the VB, resulting in the pressure minimum and the center of the VB not coinciding, but rather being below the VB.

IV. CONCLUSION

In this study, we focused on the internal separated vortex ring (VB) morphology and trajectory around the sealed cylinder axis for multiple aspect ratios in the large- Re range. By utilizing the finite element approach, we obtained abundant internal VBs and tracked the movement in a sealed cylinder. A morphological study of a separated vortex ring showed how one VB, two VBs, and three VBs emerged, expanded, shrank, and disappeared for four aspect ratios as Re increased. Axial flow characteristics along the axis, axial velocity, pressure, and vorticity distributions were given for the axisymmetric profile. The flow characteristics along the rotating axis were studied in detail, such as the axial velocity, pressure, and vorticity, which were the key physical quantity distributions causing VBs. The swirl velocity and radial pressure gradient were studied in the radial profiles at various distances h' relative to the stationary disk. The variation pattern of the paraxial streamwise length of the VBs and the distribution of the axial velocity, pressure, and vortex extremes and their corresponding positions were quantitatively studied and analyzed using Python and the theory of swirl decay.

We discovered that the exact condition for the appearance and disappearance of VBs is whether the local minimum of the natural logarithm of the axial velocity formed a closed circle near the axis. When there were multiple VBs, the first VB appeared first and disappeared last, while the second VB appeared last and disappeared first. Two VBs in the same lump domain merged together, forming a large VB as Re increased. By quantitatively studying the VB, we determined the precise Re range of the VB appearance, maximum, and disappearance. The VB axial dimension varied nonlinearly with the increase in Re . With the increase in the structure factor, the nonlinear phenomenon of the VB axial dimension variation became more complicated, not only in terms of the variations of the number of VBs but also the VB generation, splitting, merging, secondary splitting, secondary merging, and even tertiary splitting. The maximum axial dimension of the VB also increased with the increase in the structure factor. The competition of flow convergence and rotation is the key factor of the appearance and disappearance of a VB. At a relatively low range of Re , the convergence effect was stronger than the rotation effect, and the converging flow transported the angular momentum to the axis vicinity, which caused intensification of the swirl. As Re increased, the radial gradient of the pressure increased due to the increasing centrifugal force, and the suction of the pressure minimum domain generated a

VB and attracted it closer to the stationary disk. As Re continued to increase, the convergence effect was balanced with the rotation effect, the vorticity increased to the maximum value, and the VB expanded to the maximum. Subsequently, the VB shift blocked the water convergence to the axis, which diminished the axial gradient of the pressure and weakened the suction, and the VB gradually disappeared. The most striking observations are that all the locations of the local extrema of the axial velocity, pressure, and vorticity decreased in the shape of a staircase as Re increased. The major step change of the vorticity maximum caused a relatively large drop in the location of the pressure minimum, which dropped below the center of the VB, resulting in the pressure minimum and the center of the VB not coinciding, but rather being below the VB.

The discovery of the stair-step change of the VB provided evidence of the existence of a new class of fluid behavior that may offer additional freedom to design sealed cylinders by choosing aspect ratios. Furthermore, it provided insight into controlling the vortices, predicting the internal vortex movement trajectories in sealed cylinder fluids, and uncovering other as yet unknown vortex behaviors, which is vital in the science and engineering fields.

ACKNOWLEDGMENTS

We thank Peng Tan, Jie Zheng, Shaosong Zhou, Xiaohua Yuan, Wenjuan Wang, Yangxue Guo, Xueying Li, Lingchun Jia, and Jianjun Zhang for their assistance and fruitful discussions. We acknowledge the financial support of the National Natural Science Foundation of China (Grant Nos. 12172212, 11672177, and 11747080), the Science and Technology Development Special Fund Project of Shanghai Ocean University (No. A2-2006-00-200220), and the Startup Foundation for Doctor of Shanghai Ocean University (No. A2-0203-00-100375). J.P.H. acknowledges the support from the National Natural Science Foundation of China (Grant Nos. 11725521 and 12035004) and the Science and Technology Commission of Shanghai Municipality (Grant No. 20JC1414700).

AUTHOR DECLARATIONS

Conflict of Interest

The authors have no conflicts to disclose.

Author Contributions

Cong Li 李丛: Conceptualization (lead); Data curation (lead); Formal analysis (lead); Funding acquisition (equal); Investigation (lead); Methodology (lead); Project administration (lead); Resources (lead); Software (lead); Supervision (equal); Validation (equal); Visualization (lead); Writing – original draft (lead); Writing – review & editing (lead). **Jiping Huang**: Conceptualization (lead); Data curation (lead); Formal analysis (equal); Funding acquisition (equal); Investigation (lead); Methodology (lead); Project administration (lead); Resources (equal); Software (equal); Supervision (lead); Validation (equal); Visualization (equal); Writing – original draft (lead); Writing – review & editing (lead). **Wei Juan Fu**: Conceptualization (equal); Data curation (lead); Investigation (lead); Software (equal); Visualization (equal); Writing – original draft (equal). **Ge Song**: Conceptualization (equal); Formal analysis (equal); Funding acquisition (equal); Investigation (lead); Methodology (equal); Software (equal); Supervision (equal);

Writing – original draft (supporting). **Ying Li Chang**: Conceptualization (equal); Formal analysis (equal); Methodology (equal); Supervision (equal); Visualization (equal). **Zigen Song**: Investigation (equal); Methodology (equal); Visualization (equal).

DATA AVAILABILITY

The data that support the findings of this study are available from the corresponding author upon reasonable request.

REFERENCES

- J. B. Nuttall, "Axial flow in a vortex," *Nature* **172**, 582–583 (1953).
- M. V. Dyke, "Swirling flows: Vortex flow in nature and technology," *Science* **224**, 730–731 (1984).
- M. D. Graham, "Turbulence spreads like wildfire," *Nature* **526**, 508–509 (2015).
- I. V. Naumov, M. A. Herrada, B. R. Sharifullin, and V. N. Shtern, "Slip at the interface of a two-fluid swirling flow," *Phys. Fluids* **30**, 074101 (2018).
- I. V. Naumov, S. G. Skripkin, G. E. Gusev, and V. N. Shtern, "Hysteresis in a two-liquid whirlpool," *Phys. Fluids* **34**, 032108 (2022).
- M. Sharma and A. Sameen, "On the correlation between vortex breakdown bubble and planar helicity in Vogel-Escudier flow," *J. Fluid Mech.* **888**, A6 (2020).
- C. Cummins, M. Seale, A. Macente, D. Certini, E. Mastropaolo, I. M. Viola, and N. Nakayama, "A separated vortex ring underlies the flight of the dandelion," *Nature* **562**, 414–418 (2018).
- Z. G. Song and J. Xu, "Self-/mutual-symmetric rhythms and their coexistence in a delayed half-center oscillator of the cpg neural system," *Nonlinear Dyn.* **108**, 2595 (2022).
- C. Z. Fan, Y. Gao, and J. P. Huang, "Shaped graded materials with an apparent negative thermal conductivity," *Appl. Phys. Lett.* **92**, 251907 (2008).
- J. P. Huang, *Theoretical Thermotics: Transformation Thermotics and Extended Theories for Thermal Metamaterials* (Springer, Berlin, 2020).
- L. J. Xu and J. P. Huang, "Active thermal wave cloak," *Chin. Phys. Lett.* **37**, 120501 (2020).
- S. Yang, J. Wang, G. L. Dai, F. B. Yang, and J. P. Huang, "Controlling macroscopic heat transfer with thermal metamaterials: Theory, experiment and application," *Phys. Rep.* **908**, 1–65 (2021).
- B. Y. Tian, J. Wang, G. L. Dai, X. P. Ouyang, and J. P. Huang, "Thermal meta-devices with geometrically anisotropic heterogeneous composites," *Int. J. Heat Mass Transfer* **174**, 121312 (2021).
- I. V. Naumov, B. R. Sharifullin, and V. N. Shtern, "Vortex breakdown in the lower fluid of two-fluid swirling flow," *Phys. Fluids* **32**, 014101 (2020).
- A. Y. Gelfgat, P. Z. Bar-Yoseph, and A. Solan, "Stability of confined swirling flow with and without vortex breakdown," *J. Fluid Mech.* **311**, 1–36 (1996).
- C. Cummins, I. M. Viola, E. Mastropaolo, and N. Nakayama, "The effect of permeability on the flow past permeable disks at low Reynolds numbers," *Phys. Fluids* **29**, 097103 (2017).
- M. P. Escudier, "Observations of the flow produced in a cylindrical container by a rotating endwall," *Exp. Fluids* **2**, 189–196 (1984).
- J. N. Sørensen and E. A. Christensen, "Direct numerical simulation of rotating fluid flow in a closed rotor-stator cavity," *Phys. Fluids* **7**, 764–778 (1995).
- A. Spohn, M. Mory, and E. J. Hopfinger, "Experiments on vortex breakdown in a confined flow generated by a rotating disc," *J. Fluid Mech.* **370**, 73–99 (1998).
- P. M. Gresho and R. L. Sani, *Incompressible Flow and the Finite Element Method. Vol. II: Isothermal Laminar Flow* (John Wiley & Sons, New York, 1998).
- O. Lucca-Negro and T. O'Doherty, "Vortex breakdown: A review," *Prog. Energy Combust. Sci.* **27**, 431–481 (2001).
- J. M. Lopez, F. Marques, and J. Shen, "An efficient spectral-projection method for the navier-stokes equations in cylindrical geometries," *J. Comput. Phys.* **176**, 384–401 (2002).
- V. L. Okulov, I. V. Naumov, and J. N. Sørensen, "Self-organized vortex multiplets in swirling flow," *Tech. Phys. Lett.* **34**, 675–678 (2008).

- ²⁴B. Launder, S. Poncet, and E. Serre, “Laminar, transitional, and turbulent flows in rotor-stator cavities,” *Annu. Rev. Fluid Mech.* **42**, 229–248 (2010).
- ²⁵C. Li, J. Y. Huang, Q. G. Tang, J. P. Huang, J. W. Zhang, and L. W. Zhou, “Internal microstructures in shearing giant electrorheological fluids,” *Soft Matter* **8**, 5250–5255 (2012).
- ²⁶H. K. Moffatt, “Helicity and singular structures in fluid dynamics,” *Proc. Natl. Acad. Sci. U. S. A.* **111**, 3663–3670 (2014).
- ²⁷F. Kabinejadian, D. N. Ghista, B. Su, M. K. Nezhadian, L. P. Chua, J. H. Yeo, and H. L. Leo, “In vitro measurements of velocity and wall shear stress in a novel sequential anastomotic graft design model under pulsatile flow conditions,” *Med. Eng. Phys.* **36**, 1233–1245 (2014).
- ²⁸R. N. Bardakov and Y. Chashechkin, “Formation of a regular sequence of vortex loops around a rotating disk in stratified fluid,” *Fluid Dyn.* **52**, 337–344 (2017).
- ²⁹M. Vanierschot, “On the dynamics of the transition to vortex breakdown in axisymmetric inviscid swirling flows,” *Eur. J. Mech. B Fluids* **65**, 65–69 (2017).
- ³⁰M. N. Xiao, H. S. Dou, C. Y. Wu, Z. C. Zhu, X. F. Zhao, S. Y. Chen, H. L. Chen, and Y. K. Wei, “Analysis of vortex breakdown in an enclosed cylinder based on the energy gradient theory,” *Eur. J. Mech. B Fluids* **71**, 66–76 (2018).
- ³¹D. Samantaray and M. K. Das, “High Reynolds number incompressible turbulent flow inside a lid-driven cavity with multiple aspect ratios,” *Phys. Fluids* **30**, 075107 (2018).
- ³²C. Q. Liu, Y. S. Gao, S. L. Tian, and X. R. Dong, “Rortex—A new vortex vector definition and vorticity tensor and vector decompositions,” *Phys. Fluids* **30**, 035103 (2018).
- ³³S. Mulligan, G. De Cesare, J. Casserly, and R. Sherlock, “Understanding turbulent free-surface vortex flows using a Taylor-Couette flow analogy,” *Sci. Rep.* **8**, 824 (2018).
- ³⁴H. S. Dou, S. Zhang, H. Yang, T. Setoguchi, and Y. Kinoue, “Effect of rotational speed on the stability of two rotating side-by-side circular cylinders at low Reynolds number,” *J. Therm. Sci.* **27**, 125–134 (2018).
- ³⁵M. Kemp, “Leonardo da Vinci’s laboratory: Studies in flow,” *Nature* **571**, 322–323 (2019).
- ³⁶B. R. Zheng, M. Xue, and C. Ge, “Dynamic evolution of vortex structures induced by tri-electrode plasma actuator,” *Chin. Phys. B* **29**, 024704 (2020).
- ³⁷I. V. Naumov, B. R. Sharifullin, M. A. Tsoy, and V. N. Shtern, “Dual vortex breakdown in a two-fluid confined flow,” *Phys. Fluids* **32**, 061706 (2020).
- ³⁸L. Carrión, I. V. Naumov, B. R. Sharifullin, M. A. Herrada, and V. N. Shtern, “Mechanism of disappearance of vortex breakdown in a confined flow,” *J. Eng. Thermophys.* **29**, 49–66 (2020).
- ³⁹C. J. Crowley, M. C. Krygier, D. Borrero-Echeverry, R. O. Grigoriev, and M. F. Schatz, “A novel subcritical transition to turbulence in Taylor-Couette flow with counter-rotating cylinders,” *J. Fluid Mech.* **892**, A12 (2020).
- ⁴⁰D. J. Case, J. R. Angilella, and A. E. Motter, “Spontaneous oscillations and negative-conductance transitions in microfluidic networks,” *Sci. Adv.* **6**, eaay6761 (2020).
- ⁴¹J. Dély, *Three-Dimensional Separated Flow Topology: Critical Points, Separation Lines and Vortical Structures* (John Wiley & Sons, Hoboken, 2013).
- ⁴²M. Sharma and A. Sameen, “Synopsis of Vogel-Escudier flow,” *Phys. Fluids* **33**, 064105 (2021).
- ⁴³A. van Reenen, A. M. de Jong, and M. W. J. Prins, “Accelerated particle-based target capture—the roles of volume transport and near-surface alignment,” *J. Phys. Chem. B* **117**, 1210–1218 (2013).
- ⁴⁴S. Shin, J. T. Ault, and H. A. Stone, “Flow-driven rapid vesicle fusion via vortex trapping,” *Langmuir* **31**, 7178–7182 (2015).
- ⁴⁵S. Kim, H. Park, H. A. Gruszewski, D. G. Schmale, and S. Jung, “Vortex-induced dispersal of a plant pathogen by raindrop impact,” *Proc. Natl. Acad. Sci. U. S. A.* **116**, 4917–4922 (2019).
- ⁴⁶M. S. Krieger, S. Sinai, and M. A. Nowak, “Turbulent coherent structures and early life below the Kolmogorov scale,” *Nat. Commun.* **11**, 2192 (2020).
- ⁴⁷S. Hattori, M. Moris, K. Shinozaki, K. Ishii, and T. Verbiest, “Vortex-induced harmonic light scattering of porphyrin J-aggregates,” *J. Phys. Chem. B* **125**, 2690–2695 (2021).
- ⁴⁸M. T. F. Rodrigues, P. M. Ajayan, and G. G. Silva, “Fast vortex-assisted self-assembly of carbon nanoparticles on an air-water interface,” *J. Phys. Chem. B* **117**, 6524–6533 (2013).
- ⁴⁹C. J. Schram, R. J. Smyth, L. S. Taylor, and S. P. Beaudoin, “Understanding crystal growth kinetics in the absence and presence of a polymer using a rotating disk apparatus,” *Cryst. Growth Des.* **16**, 2640–2645 (2016).
- ⁵⁰B. Ji, J. Wang, X. Luo, K. Miyagawa, L. Z. Xiao, X. Long, and Y. Tsujimoto, “Numerical simulation of cavitation surge and vortical flows in a diffuser with swirling flow,” *J. Mech. Sci. Technol.* **30**, 2507–2514 (2016).
- ⁵¹F. Wu, X. X. Che, Z. Y. Huang, H. J. Duan, X. X. Ma, and W. J. Zhou, “Numerical study on the gas-solid flow in a spouted bed installed with a controllable nozzle and a swirling flow generator,” *ACS Omega* **5**, 1014–1024 (2020).
- ⁵²L. Carrión, I. V. Naumov, B. R. Sharifullin, M. A. Herrada, and V. N. Shtern, “Formation of dual vortex breakdown in a two-fluid confined flow,” *Phys. Fluids* **32**, 104107 (2020).
- ⁵³V. N. Shtern, *Cellular Flows* (Cambridge University Press, Cambridge, 2018).
- ⁵⁴I. V. Naumov, S. G. Skripkin, and V. N. Shtern, “Counterflow slip in a two-fluid whirlpool,” *Phys. Fluids* **33**, 061705 (2021).
- ⁵⁵S. Sharma, P. B. Sachan, N. Kumar, R. Ranjan, S. Kumar, and K. Poddar, “Vortex breakdown control using varying near axis swirl,” *Phys. Fluids* **33**, 093606 (2021).
- ⁵⁶S. G. Skripkin, B. R. Sharifullin, I. V. Naumov, and V. N. Shtern, “Dual vortex breakdown in a two-fluid whirlpool,” *Sci. Rep.* **11**, 23085 (2021).
- ⁵⁷I. V. Naumov, M. A. Herrada, B. R. Sharifullin, and V. N. Shtern, “Hysteretic growth and decay of a waterspout column,” *Phys. Rev. Fluids* **3**, 024701 (2018).
- ⁵⁸L. Carrión, M. A. Herrada, and V. N. Shtern, “Topology changes in a water-oil swirling flow,” *Phys. Fluids* **29**, 032109 (2017).
- ⁵⁹L. Carrión, M. A. Herrada, and V. N. Shtern, “Topology and stability of a water-soybean-oil swirling flow,” *Phys. Rev. Fluids* **2**, 024702 (2017).
- ⁶⁰V. N. Shtern and A. A. Borissov, “Counterflow driven by swirl decay,” *Phys. Fluids* **22**, 063601 (2010).
- ⁶¹V. N. Shtern, M. M. Torregrosa, and M. A. Herrada, “Effect of swirl decay on vortex breakdown in a confined steady axisymmetric flow,” *Phys. Fluids* **24**, 043601 (2012).